ЖЭТФ, 2002, том 122, вып. 1 (7), стр. 17–32

CROSS-SECTION OF THE MUON-NUCLEAR INELASTIC INTERACTION

***A. V. Butkevich*[*], *S. P. Mikheyev*[**]**

Institute for Nuclear Research, Russian Academy of Sciences
117312, Moscow, Russia

Submitted 6 February 2002

It is shown that the combination of the structure functions F_2 predicted by the CKMT model at low and moderate values of Q^2 and the MRS99 parton distribution functions at high Q^2 gives a good description of the data over the complete measured region of x and Q^2. Using these structure functions, the main characteristics of the muon-nuclear inelastic scattering are calculated. Nuclear effects and contributions of the neutral current and the γ–Z interference are taken into account.

PACS: 13.10.+q, 13.60.-r

1. INTRODUCTION

Muon inelastic scattering off nuclei plays an important role in muon propagation through matter. In this process, the muon can loose a significant part of its energy and can be scattered at large angles. Therefore, the muon-nuclear inelastic scattering is of interest in numerous applications related to the muon transport in matter, in particular, in calculations of the muon intensity at large depth of matter, the muon-induced hadron flux underground, the background produced by atmospheric muons in underground neutrino experiments, etc.

Several models [1–4] have been developed to describe the muon-nuclear inelastic interaction; however, uncertainties of this process are much larger than for purely electromagnetic interactions. The reason is that the bulk of this process is characterized by a low squared four-momentum transfer Q^2. The smallness of Q^2 does not allow us to use the perturbative QCD (pQCD) to calculate the nuclear structure function, and phenomenological models such as the Regge or General Vector Dominance Model (GVDM) must be used. The parameterization of the nucleon structure functions obtained in these models depends on free parameters that can be determined from a fit of experimental data and can be applied in the range $Q^2 \leq 1$–3 GeV^2. This range is often referred to as photoproduction. But these models fail to describe deep inelastic scattering (DIS) data at high Q^2. The pQCD (NLO QCD) gives a good description of the structure functions at $Q^2 \geq 3$ GeV^2. A model combining various aspects of these approaches is therefore needed to describe the Q^2 behavior of nucleon structure functions over the entire range from photoproduction to DIS.

The widely used approximation [4] of the muon photonuclear cross-section was obtained twenty years ago in the GVDM framework. Experimental data for $Q^2 \leq 100$ GeV^2 and $x \geq 0.01$ were used to determine the parameters. Recently, precise data [5] on structure functions in wide ranges of Q^2 ($0.045 \leq Q^2 \leq 10^4$ GeV^2) and x ($10^{-6} \leq x \leq 0.98$) have been obtained and new nuclear effects (antishadowing and EMC effects) were observed.

The main goal of this paper is the calculation of the muon-nuclear inelastic cross-section, based on the modern nucleon structure functions and on the present knowledge of nuclear effects.

The paper is organized as follows. In Sec. 2, we give the general relations and definitions used in describing the neutral current charged lepton–nucleon scattering. The procedure of the calculation of the nucleon structure function using the CKMT Regge model [6] and the MRS99 parton distribution function [7] is described in Sec. 3. In Sec. 4, nuclear effects and their parameterization are described. The total cross-section, the muon

[*]E-mail: butkevic@al20.inr.troitsk.ru
[**]E-mail: mikheyev@pcbai10.inr.ruhep.ru

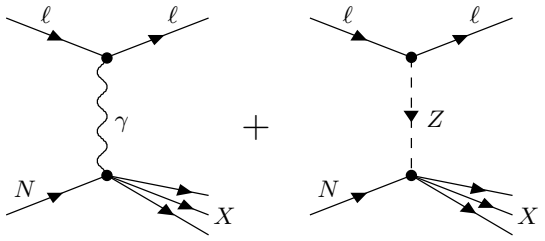

Fig. 1. Schematic diagrams for the neutral current charged lepton scattering off nucleon

energy loss, and the angular distributions of scattered muons are given in Sec. 5. In Conclusions, we summarize the main results of the paper.

2. NEUTRAL CURRENT CHARGED LEPTON–NUCLEON SCATTERING CROSS-SECTION

The cross-section of the neutral current charged lepton scattering off nucleon,

$$l(k) + N(p) \to l(k') + X(p'), \tag{1}$$

is given by the sum of contributions of the processes shown in Fig. 1 Here, $k(E, \mathbf{k})$ and $k'(E', \mathbf{k}')$ are the initial and final lepton four-momenta, $q = k - k'$ is the virtual photon or Z-boson momentum, p and p' are the initial nucleon momentum and the total momentum of the final hadrons X, respectively. This process can be described by the transferred four-momentum Q^2, the Bjorken variable x, and the lepton energy loss ν (or inelasticity y) defined as

$$\begin{aligned} &Q^2 = -q^2 = (k - k')^2, \\ &x = \frac{Q^2}{2pq}, \quad \nu = \frac{qp}{M}, \quad y = \frac{pq}{pk}. \end{aligned} \tag{2}$$

In laboratory system

$$\begin{aligned} &Q^2 = 2(EE' - \mathbf{k}\cdot\mathbf{k}') - 2m^2, \\ &x = \frac{Q^2}{2M\nu}, \quad \nu = E - E', \quad y = \frac{\nu}{E}, \end{aligned} \tag{3}$$

where M and m are the nucleon and lepton masses, respectively.

The general form of the differential cross-section for the scattering of a charge nonpolarized lepton on a nonpolarized nucleon, summed over the final lepton polarizations, can be expressed as

$$\frac{d^2\sigma^{l^-,l^+}}{d\nu\, dQ^2} = \frac{2\pi\alpha^2}{Q^4E^2} \times \\ \times\Big[E^{l^-,l^+}(x,Q^2) - I^{l^-,l^+}(x,Q^2) + Z^{l^-,l^+}(x,Q^2)\Big], \tag{4}$$

where

$$E^{l^-,l^+} = 2xF_1^{el}(x,Q^2)Y_1 + F_2^{el}(x,Q^2)Y_2, \tag{5}$$

$$I^{l^-,l^+} = P_Z\Big\{g_V\Big[2xF_1^I(x,Q^2)Y_1 + F_2^I(x,Q^2)Y_2\Big] \mp \\ \mp g_A xF_3^I(x,Q^2)Y_3\Big\}, \tag{6}$$

$$Z^{l^-,l^+} = P_Z^2\Big\{(g_V^2 + g_A^2)\Big(2xF_1^Z(x,Q^2)Y_1 + \\ + F_2^Z(x,Q^2)Y_2\Big) \mp 2g_V g_A xF_3^Z(x,Q^2)Y_3\Big\}, \tag{7}$$

and

$$\begin{aligned} Y_1 &= \left(Q^2 - 2m^2\right)\frac{\nu}{Q^2}, \\ Y_2 &= \left[2E(E-\nu) - \frac{Q^2}{2}\right]\frac{1}{\nu}, \\ Y_3 &= 2E - \nu. \end{aligned} \tag{8}$$

Here, the term P_Z accounts for the Z^0 propagator,

$$P_Z = \frac{G}{\sqrt{2}}\,\frac{Q^2}{2\pi\alpha}\,\frac{m_Z^2}{Q^2 + m_Z^2}, \tag{9}$$

where $G/\sqrt{2}$ is the Fermi constant, $\alpha = 1/137$ is the fine structure constant, and m_Z is Z-boson mass. The lepton weak coupling constants g_V and g_A are

$$g_V = -\frac{1}{2} + 2\sin^2\theta_W, \quad g_A = -\frac{1}{2}, \tag{10}$$

where θ_W is the Weinberg angle.

The functions $F_i^{el,Z}$ are the electromagnetic (γ-exchange) and neutral current (Z-exchange) structure functions, respectively. The functions F_i^I correspond to the decomposition over invariant functions of the tensor (γ–Z interference)

$$W^I \approx \sum\Big\{\Big\langle p'|J_\alpha^{el}|p\Big\rangle\Big\langle p|J_\beta^Z|p'\Big\rangle + \\ + \Big\langle p'|J_\alpha^Z|p\Big\rangle\Big\langle p|J_\beta^{el}|p'\Big\rangle\Big\}\delta(p' - p - q). \tag{11}$$

The upper sign in Eqs. (6) and (7) corresponds to the lepton scattering (e^-, μ^-) and the lower sign is for the antilepton (e^+, μ^+) scattering.

The term proportional to the function F_3^I is due to the interference between the electromagnetic scattering amplitude and the axial-vector current weak interaction amplitude. The amplitudes have opposite C

parities, and the corresponding terms therefore have opposite signs for the lepton and the antilepton scattering. At low Q^2, the γ–Z interference term is much smaller than the γ-exchange one, but it increases linearly with Q^2 (Eq. (9)) and becomes comparable to the γ-exchange term at $Q^2 \approx 10^3$ GeV^2.

In terms of the parton distribution in the LO-approximation, the structure functions can be written as

$$F_1^{el} = \frac{1}{2}\sum e_q^2 \left(f_q + f_{\bar{q}}\right), \tag{12}$$

$$F_2^{el} = x\sum e_q^2 \left(f_q + f_{\bar{q}}\right), \tag{13}$$

$$F_1^{Z} = \frac{1}{2}\sum \left(v_q^2 + a_q^2\right)\left(f_q + f_{\bar{q}}\right), \tag{14}$$

$$F_2^{Z} = x\sum \left(v_q^2 + a_q^2\right)\left(f_q + f_{\bar{q}}\right), \tag{15}$$

$$F_3^{Z} = 2\sum v_q a_q \left(f_q - f_{\bar{q}}\right), \tag{16}$$

$$F_1^{I} = \sum e_q v_q \left(f_q + f_{\bar{q}}\right), \tag{17}$$

$$F_2^{I} = 2x\sum e_q v_q \left(f_q + f_{\bar{q}}\right), \tag{18}$$

$$F_3^{I} = 2\sum e_q a_q \left(f_q - f_{\bar{q}}\right). \tag{19}$$

Here, f_q and $f_{\bar{q}}$ are parton distribution functions in the proton; e_q, v_q, and a_q are the charge, vector, and axial-vector week couplings of quarks. For the up-quarks (u, c, t) they are given by

$$e_{u,c,t} = \frac{2}{3}, \quad v_{u,c,t} = \frac{1}{2} - \frac{4}{3}\sin^2\theta_W, \quad a_{u,c,t} = \frac{1}{2} \tag{20}$$

and for the down-quarks (d, s, b),

$$\begin{aligned} e_{d,s,b} &= -\frac{1}{3}, \quad v_{d,s,b} = -\frac{1}{2} + \frac{2}{3}\sin^2\theta_W, \\ a_{d,s,b} &= -\frac{1}{2}. \end{aligned} \tag{21}$$

It can be seen from Eqs. (4) and (9) that the main contribution to the total cross-section is due to photoproduction (a low-Q^2 process); however, at a fixed outgoing muon energy, the large scattering angle corresponds to high Q^2,

$$\cos\theta = \left(EE' - Q^2/2 - m^2\right)/|\mathbf{k}||\mathbf{k}'|. \tag{22}$$

Therefore, the calculation of the muon scattering at large angles requires the knowledge of the behavior of the nucleon structure functions in the wide range of $Q^2 \approx 0.01$–10^6 GeV^2.

3. LOW- AND HIGH-Q^2 APPROXIMATIONS OF THE NUCLEON STRUCTURE FUNCTIONS

At high Q^2, the QCD predictions for the nucleon structure functions are obtained by solving the DGLAP evolution equations at the NLO approximation in the $\overline{\text{MS}}$ or DIS schemes. These equations yield the parton distribution functions at all values of Q^2 provided these functions are given as a function of x at some input scale $Q_0^2 = 1.2$–5 GeV^2. The latest global fits performed by several groups (MRS99 [7], GRV98 [8], and CTEQ5 [9]) give a good description of the experimental data. At Q^2 below Q_0^2, the perturbative QCD fails to describe data and phenomenological nonperturbative (GVDM or Regge) models are required. A considerable number of nonperturbative models have been developed recently [10–12]. These models predict the correct limit of F_2 at $Q^2 = 0$ and give a good description of the structure functions at low and medium Q^2. Thus, neither the nonperturbative approaches nor pQCD can be expected to describe the Q^2 behavior of the structure functions over the entire range from photoproduction to DIS. A number of models combining QCD and phenomenological approaches have been developed to describe data in the transition region of Q^2 (see review [13]). In this paper, we use the CKMT model [6] at low and moderate Q^2 and the MRS99 fit of the parton distribution function [7] at high Q^2.

The CKMT model proposes the following parameterization of the proton structure function F_2^p:

$$F_2^p(x, Q^2) = F_S^p(x, Q^2) + F_{NS}^p(x, Q^2). \tag{23}$$

The singlet term

$$F_S^p(x, Q^2) = A_S\, x^{-\Delta(Q^2)}\,(1-x)^{n(Q^2)+4} \times \left(\frac{Q^2}{Q^2+a}\right)^{1+\Delta(Q^2)} \tag{24}$$

corresponds to the Pomeron contribution that which determines the small-x behavior of sea quarks and gluons. The dependence of the effective intercept of the Pomeron Δ on Q^2 is parameterized as

$$\Delta(Q^2) = \Delta_0\left(1 + \frac{2Q^2}{Q^2+d}\right). \tag{25}$$

The $x \to 1$ behavior of $F_S(x, Q^2)$ is determined by the function

$$n(Q^2) = \frac{3}{2}\left(1 + \frac{Q^2}{Q^2+c}\right). \tag{26}$$

The parameterization of the nonsinglet term, which corresponds to the secondary (f,A_2) reggeon (valence quark) contribution, is given by

$$F_{NS}^{p}(x,Q^2) = Bx^{(1-\alpha_R)}\,(1-x)^{n(Q^2)} \times \times \left(\frac{Q^2}{Q^2+b}\right)^{\alpha_R}, \quad (27)$$

where the behavior as $x \to 0$ is determined by the secondary reggeon intercept α_R. The valence quark distribution can be separated into contributions of the u and d valence quarks by replacing

$$F_{NS}^{p}(x,Q^2) = xU_V(x,Q^2) + xD_V(x,Q^2), \quad (28)$$

where

$$xU_V(x,Q^2) = B_u x^{(1-\alpha_R)}\,(1-x)^{n(Q^2)} \times \times \left(\frac{Q^2}{Q^2+b}\right)^{\alpha_R}, \quad (29)$$

$$xD_V(x,Q^2) = B_d x^{(1-\alpha_R)}\,(1-x)^{n(Q^2)+1} \times \times \left(\frac{Q^2}{Q^2+b}\right)^{\alpha_R}, \quad (30)$$

and B_u and B_d are fixed at $Q^2 = Q_0^2$ by the normalization conditions for valence quarks in proton:

$$\int\limits_0^1 \frac{1}{x}\left[xU_V(x,Q^2)\right]dx = 2e_u^2, \qquad \int\limits_0^1 \frac{1}{x}\left[xD_V(x,Q^2)\right]dx = e_d^2. \quad (31)$$

The limit of $Q^2 = 0$ corresponds to the interaction of real photons. The total cross-section for real photons can be written as

$$\sigma_{\gamma p}^{tot}(\nu) = \left[\frac{4\pi^2\alpha}{Q^2}F_2(x,Q^2)\right]_{Q^2=0}. \quad (32)$$

We see from Eqs. (23), (24), and (28) that $F_2 \approx Q^2$ as $Q^2 \to 0$ for a fixed ν. Thus, the parameterization

$$\sigma_{\gamma p}^{tot}(\nu) = 4\pi^2\alpha\Big[A_s a^{-1-\Delta_0}(2M\nu)^{\Delta_0} + + (B_u + B_d)b^{-\alpha_R}(2M\nu)^{\alpha_R-1}\Big] \quad (33)$$

applies in the CKMT model.

In this way, we find parameterizations of both the F_2^p and γp cross-sections with seven free parameters: $a, b, c, d, \Delta_0, \alpha_R$, and A_S. To determine the parameters, we have made a joint fit of the $\sigma_{\gamma p}^{tot}$ data and the NMC, E665, SLAC, ZEUS, and H1 data on the proton structure function F_2 in the regions $0.11 \le Q^2 \le 5.5$ GeV^2 and $10^{-6} \le x \le 0.98$ [5]. As the initial condition for the values of different parameters, we used those obtained in the previous fit in Ref. [6]. A global fit results in the following values of the parameters (all dimensional parameters are expressed in GeV^2):

$$a = 0.2513, \quad b = 0.6186, \quad c = 3.0292, \quad d = 1.4817,$$

$$\Delta_0 = 0.0988, \quad \alpha_R = 0.4056, \quad A_S = 0.12.$$

The values of the parameters $B_u = 1.2437$ and $B_d = 0.1853$ were determined from the normalization conditions for valence quarks (at $Q_0^2 = 2$ GeV^2). The quality of the description of all experimental data is very good and $\chi^2/\text{d.o.f.} = 754.8/600$, where only the statistical errors have been used. Recently, a modified version of the CKMT model with the new data on F_2^p at low Q^2 was published [14]. The values of the main parameters are in a good agreement with those obtained in the present work.

To calculate F_2 in the entire region of Q^2, we therefore use the CKMT model at $Q^2 \le 5$ GeV^2, the MRS99 parton distribution function at $Q^2 \ge 6$ GeV^2, and a linear fit between F_2^p(CKMT) and F_2^p(MRS99) in the region $5 \le Q^2 \le 6$ GeV^2. The result of the fit of F_2^p and $\sigma_{\gamma p}^{tot}$ is shown in Figs. 2 and 3 (F_2^p versus x for different values of Q^2) and Fig. 4 (F_2^p versus Q^2 for different values of x) along with the experimental data [5, 15]. The cross-section $\sigma_{\gamma p}^{tot}$ as a function of $W^2 = M^2 + 2M\nu - Q^2$ is shown in Fig. 5 (the data from [16, 17]).

A good description of experimental data is obtained for all x and Q^2 values. We note that

a) the recent ZEUS BPT97 data [15] were not included in our fit, but are in agreement with the CKMT model prediction at $Q^2 \le 0.1$ GeV^2;

b) the rise of F_2^p at low x and low Q^2 is well described by the CKMT model with the slope $\Delta_0 = 0.0988$, while the experimental value is 0.102 ± 0.070 [15];

c) the $\sigma_{\gamma p}^{tot}$ values found by the ZEUS collaboration are the result of a phenomenologically motivated extrapolation.

In Figs. 2–5, we show the structure function F_2^p and $\sigma_{\gamma p}^{tot}$ that were obtained by Bezrukov and Bugaev [4] and were used for calculating the muon photonuclear cross-section are also shown. At $x < 10^{-3}$, the structure functions rise slower than the present data indicate. On the other hand, in the region $x > 0.01$ and $Q^2 > 5$ GeV^2, the structure functions are overestimated.

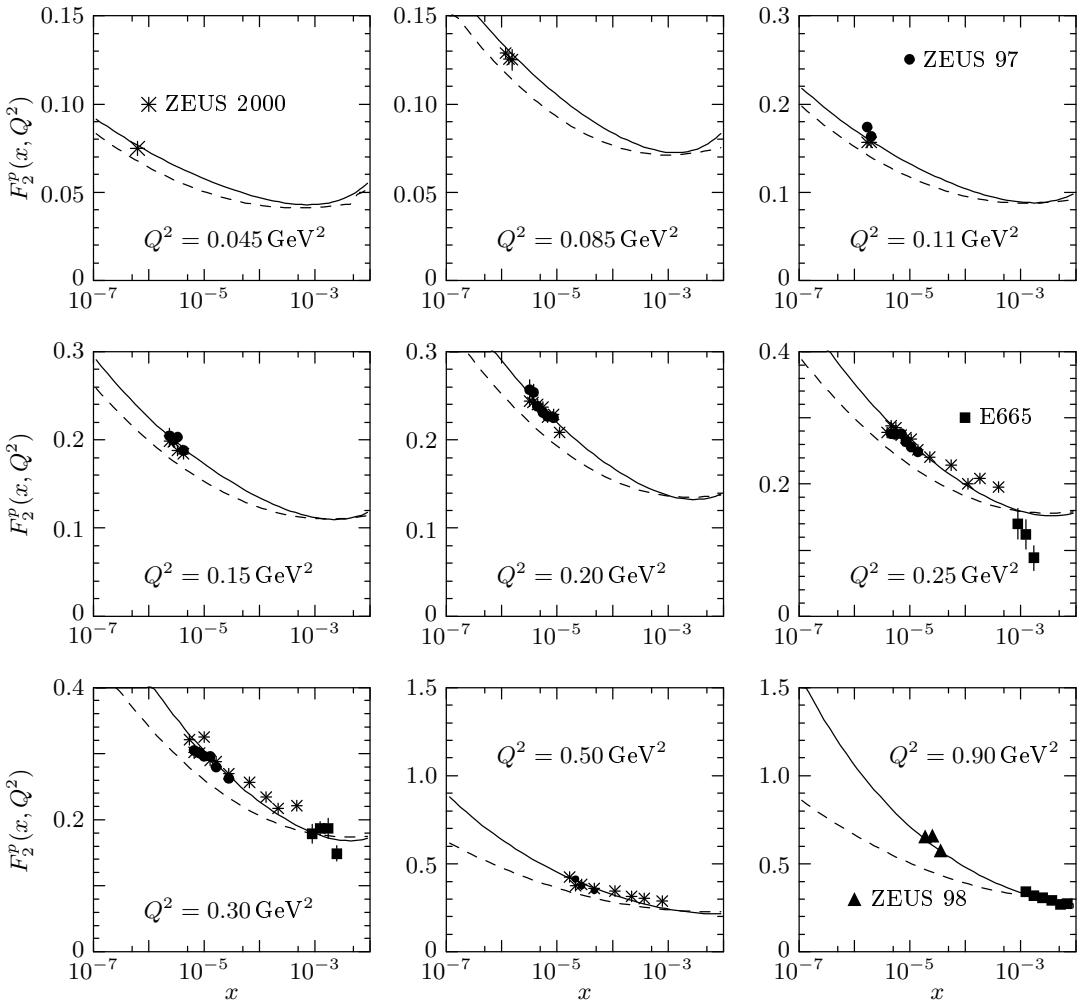

Fig. 2. The proton structure function F_2^p at low Q^2 versus x. Solid lines are our calculations using the CKMT model and dashed lines are the calculations of Bezrukov and Bugaev [4]. Points are experimental results [5, 15]

The CKMT parameterization gives separate contributions of valence quarks, sea quarks, and gluons. We used this peculiarity for parameterizing the neutron structure function F_2^n that can be extracted from the deuteron F_2^d and the proton F_2^p data using the relation

$$F_2^d = \frac{1}{2}\left[F_2^p(x) + F_2^n(x)\right] \tag{34}$$

and the Gottfried sum rule

$$S_G = \int_0^1 (F_2^p - F_2^n)\,\frac{dx}{x} = \frac{1}{3}\int_0^1 (d_V - u_V)dx - \frac{2}{3}\int_0^1 (\bar{d} - \bar{u})dx. \tag{35}$$

In the case of the $SU(2)$-symmetric sea, the parton distribution function of $\bar{d}$ is equal to that of $\bar{u}$, and therefore, $S_G = 1/3$. But the NMC collaboration [5] gives $S_G = 0.235 \pm 0.026$ at $Q^2 = 4$ GeV^2, which is significantly below $1/3$ and shows that $F_2^p(x) - F_2^n(x) \to 0$ and $F_2^n(x)/F_2^p(x) \to 1$ as $x \to 0$. Taking these results into account, the singlet term of F_2^n must be modified. Because of the isotopical invariance of the strong interaction, the nonsinglet term F_{NS}^n is

$$F_{NS}^n(x, Q^2) = \frac{1}{4}xU_V(x, Q^2) + 4xD_V(x, Q^2), \tag{36}$$

where $xU_V(x, Q^2)$ and $xD_V(x, Q^2)$ are given by

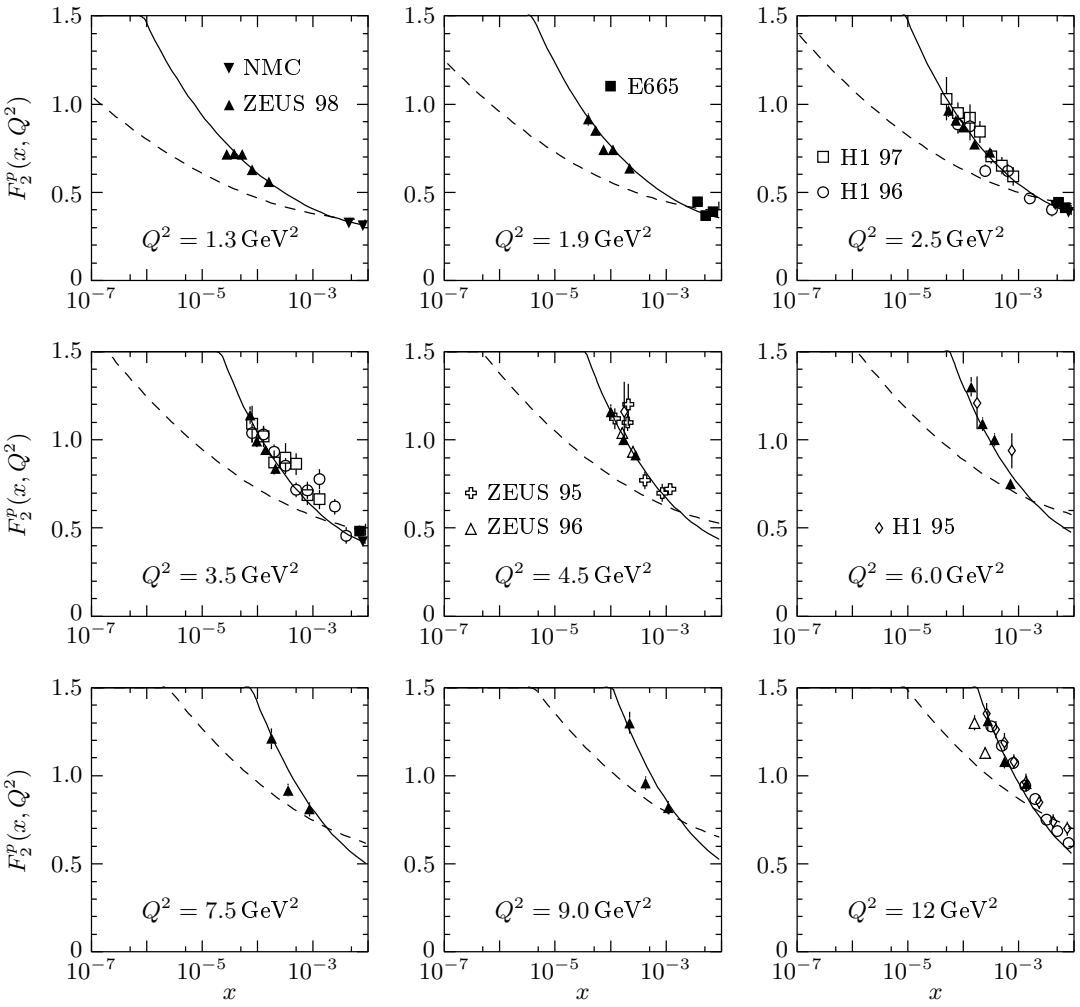

Fig. 3. The same as in Fig. 2 but at moderate Q^2

Eqs. (29) and (30). The singlet term

$$F_S^n(x,Q^2) = A_S x^{-\Delta(Q^2)}(1-x)^{n(Q^2)+\tau} \times \\ \times \left(\frac{Q^2}{Q^2+a}\right)^{1+\Delta(Q^2)} \qquad (37)$$

involves an additional free parameter τ. The value of this parameter obtained from the fit of the F_2^d data [5] in the region $Q^2 \le 5$ GeV^2 (with all the other parameters fixed by the fit of the F_2^p and $\sigma_{\gamma p}^{tot}$) is $\tau = 1.8152$. The quality of the data description is good with the value of χ^2/d.o.f. $= 611.1/453$ for the structure function F_2^d data and χ^2/d.o.f. $= 452.8/380$ for the F_2^n/F_2^p data, where only statistical errors have been used.

To calculate the structure function F_2^n in the entire region of Q^2, we used the approximation in Eqs. (36) and (37) at $Q^2 \le 5$ GeV^2, the MRS99 parton distribution function at $Q^2 \ge 6$ GeV^2, and a linear fit between F_2^n(CKMT) and F_2^n(MRS) in the transition region $5 < Q^2 < 6$ GeV^2. The structure function F_2^d (Fig. 6) and the ratio F_2^n/F_2^p (Fig. 7) versus Q^2 for different values of x are shown along with experimental data. Figure 8 shows $F_2^p - F_2^n$ versus x at $Q^2 = 4$ GeV^2. The calculations are in agreement with the NMC data [18].

For the calculation of the cross-section of lepton–nucleon scattering, the behavior of the structure function $2xF_1$ must be known in a wide range of Q^2 and x. This function can be expressed using the longitudinal structure function

$$F_L = \left(1 + \frac{4M^2x^2}{Q^2}\right) F_2 - 2xF_1. \qquad (38)$$

Then

$$2xF_1 = \frac{1}{1+R}\left(1 + \frac{4M^2x^2}{Q^2}\right) F_2, \qquad (39)$$

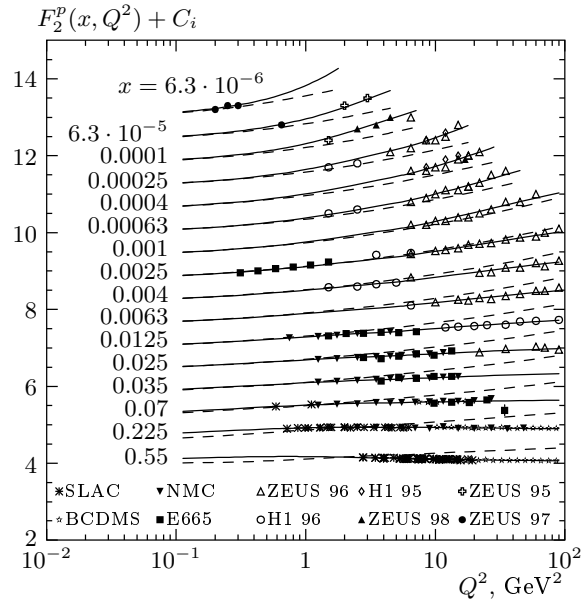

Fig. 4. The proton structure function F_2^p versus Q^2 at fixed values of x. The solid curves were obtained using the CKMT+MRS99 model and the dashed curves are the results in Ref. [4]. Data set is due to experiments [5]. For clarity, the quantity $C_i = 13.6\text{–}0.6i$ is added to F_2^p, where $i = 1(16)$ for the lowest (highest) x value

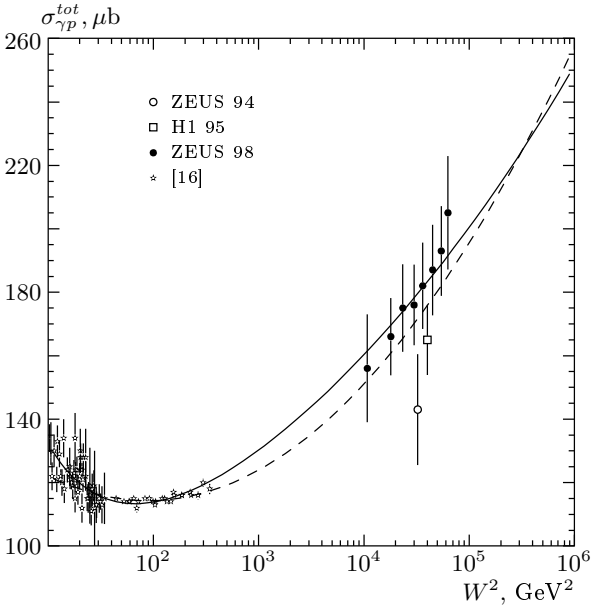

Fig. 5. The total cross-section $\sigma_{\gamma p}^{tot}$ as a function of W^2. The solid line is the result of our calculations using the combined CKMT+MRS99 model and the dashed line is taken from [4]. Experimental data are taken from [16] at low energies and from ZEUS and H1 [17] at higher energies

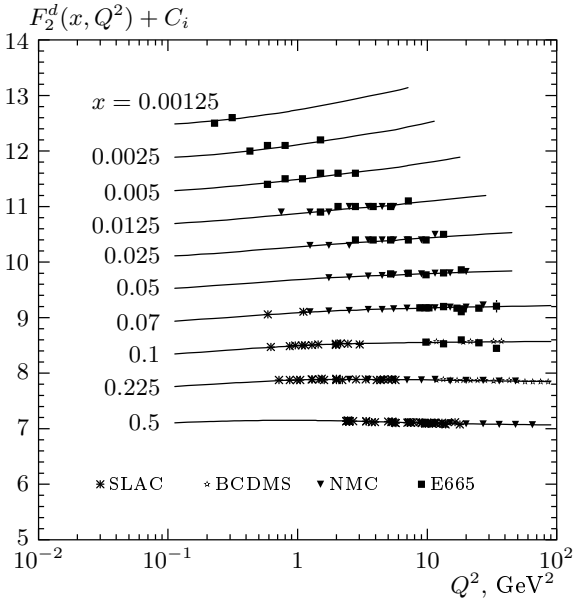

Fig. 6. The deutron structure function F_2^d versus Q^2 at fixed values of x. Data set is due to BCDMS, E665, NMC, and SLAC experiments [5]. For clarity, the quantity $C_i = 13.6\text{–}0.6i$ is added to F_2^d, where $i = 1(10)$ for the lowest (highest) x value

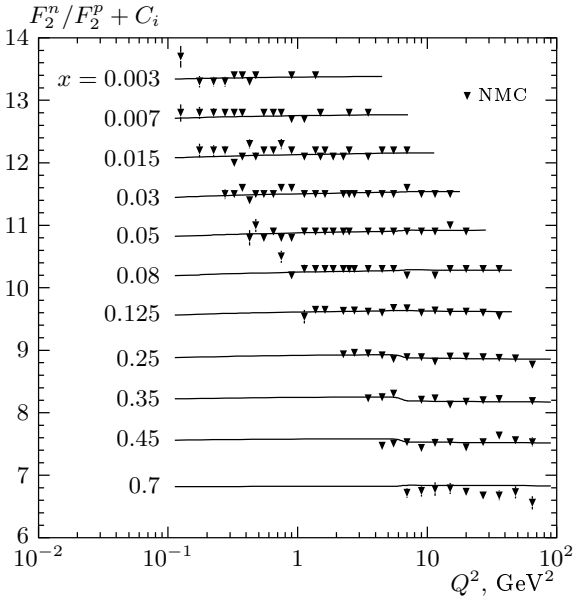

Fig. 7. The ratio of the structure functions F_2^n/F_2^p versus Q^2 at fixed values of x, as compared to NMC data [5]. For clarity, the quantity $C_i = 13.6 - 0.6i$ is added to F_2^n/F_2^p, where $i = 1(11)$ for the lowest (highest) x value

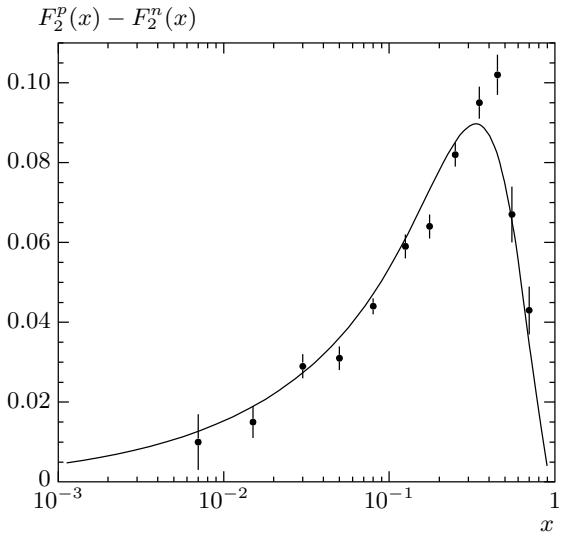

Fig. 8. The difference $F_2^p - F_2^n$ at $Q^2 = 4$ GeV^2 as a function of x, as compared to NMC data [5]

where

$$R \equiv \frac{\sigma_L}{\sigma_T} = \frac{F_L}{(1 + 4M^2x^2/Q^2)\,F_2 - F_L}. \qquad (40)$$

Perturbative QCD describes the available data on the ratio $R(x, Q^2)$ at large values of Q^2 reasonably well, but very little is known about possible extrapolations towards the region of low Q^2. In the limit as $Q^2 \to 0$, the structure function F_L must vanish as Q^4 (for fixed ν), and therefore, $R \approx Q^2$. At $x < 0.01$ and $Q^2 < 0.5$ GeV^2, the experimental results are poor. The data show a small value of R at moderate values of x and a possible increase of R as x decreases. The data come from experiments carried out with different targets (nuclei and protons), and the differences $R^A - R^p$ are consistent with zero and do not exhibit any significant dependence on x [19].

Data can be fitted by the parameterization R(SLAC98) [20]. But this fit must not be used at $Q^2 < 0.35$ GeV^2. In this region, we used the GVDM asymptotic form of R as $Q^2 \to 0$ given by [21]

$$R_{GVDM}(Q^2, x) \approx \frac{Q^2}{Q^2 + m_\rho^2},$$

where $m_\rho = 0.77$ GeV is the ρ-meson mass. At $Q^2 > Q_0^2 = 1.4$ GeV^2, the function $R(x, Q^2)$ is therefore calculated as

$$R(x, Q^2) = \begin{cases} R(\text{MRS99}) & \text{at} \quad x < 10^{-3}, \\ R(\text{SLAC98}) & \text{at} \quad x \geq 5.10^{-3}. \end{cases} \qquad (41)$$

In the region $10^{-3} < x < 5 \cdot 10^{-3}$, a linear fit between R(MRS99, $x = 10^{-3}$) and R (SLAC98, $x = 5 \cdot 10^{-3}$) is used. At $Q^2 < Q_0^2$,

$$R(x, Q^2) = R_{GVDM}(x, Q^2) = C(x)\frac{Q^2}{Q^2 + m_\rho^2}, \qquad (42)$$

where the function $C(x)$ is determined by the normalization condition at Q_0^2,

$$R_{GVDM}(x, Q_0^2) = R(x, Q_0^2), \qquad (43)$$

and the function $R(x, Q_0^2)$ is calculated using Eq. (41). Figure 9 shows the experimental values of R as a function of Q^2 in four ranges of x along with the result of the parameterization in Eqs. (41) and (42). In the region of low $Q^2 < Q_0^2$, R decreases with Q^2 at all values x, but the dependence on x is not strong (Fig. 10). However, the extrapolation of R outside the kinematical range of data (namely, as $Q^2 \to 0$ and $x \to 0$) based on the presently available data is a rather delicate problem.

In Figs. 11 and 12, we show the results of calculations of the differential cross-sections of the neutral current $e^\pm p$ scattering $d\sigma/dQ^2$ and $d\sigma/dy$ at high Q^2. The cross-section $d\sigma/dQ^2$ decreases by six orders of magnitude between $Q^2 = 400$ and 4000 GeV^2. This decrease is due to the photon propagator. The cross-section $d\sigma/dy$ is shown for different Q^2 regions. For $Q^2 > 400$ GeV^2, the bulk of the cross-section is concentrated at small values of y. For $Q^2 > 10^4$ GeV^2, the differential cross-section is approximately constant in y. The predictions using the MRS99 parton distribution function give a good description of the measured cross-sections. The neutral current scattering at high Q^2 is sensitive to the contribution of Z^0. In accordance with Eqs. (4)–(9), the Z^0 contribution reduces the e^+p (e^-p) cross-section at $Q^2 > 10^4$ GeV^2 by approximately 25 % (12 %).

4. NUCLEAR STRUCTURE FUNCTIONS

The structure functions measured for different nuclei A are found to differ from the structure functions measured on deuteron [24, 25]. The modifications are usually observed as a deviation of the ratio $r^{A/d} = F_2^A/F_2^d$ from unity, where F_2^A and F_2^d are the structure functions per nucleon measured in a nucleus and deuteron, respectively. Neglecting nuclear effects in the deuteron, F_2^d can approximately stand for an isospin averaged nucleon structure function, $F_2^N = (F_2^p + F_2^n)/2$. Different nuclear effects are observed in different regions of x.

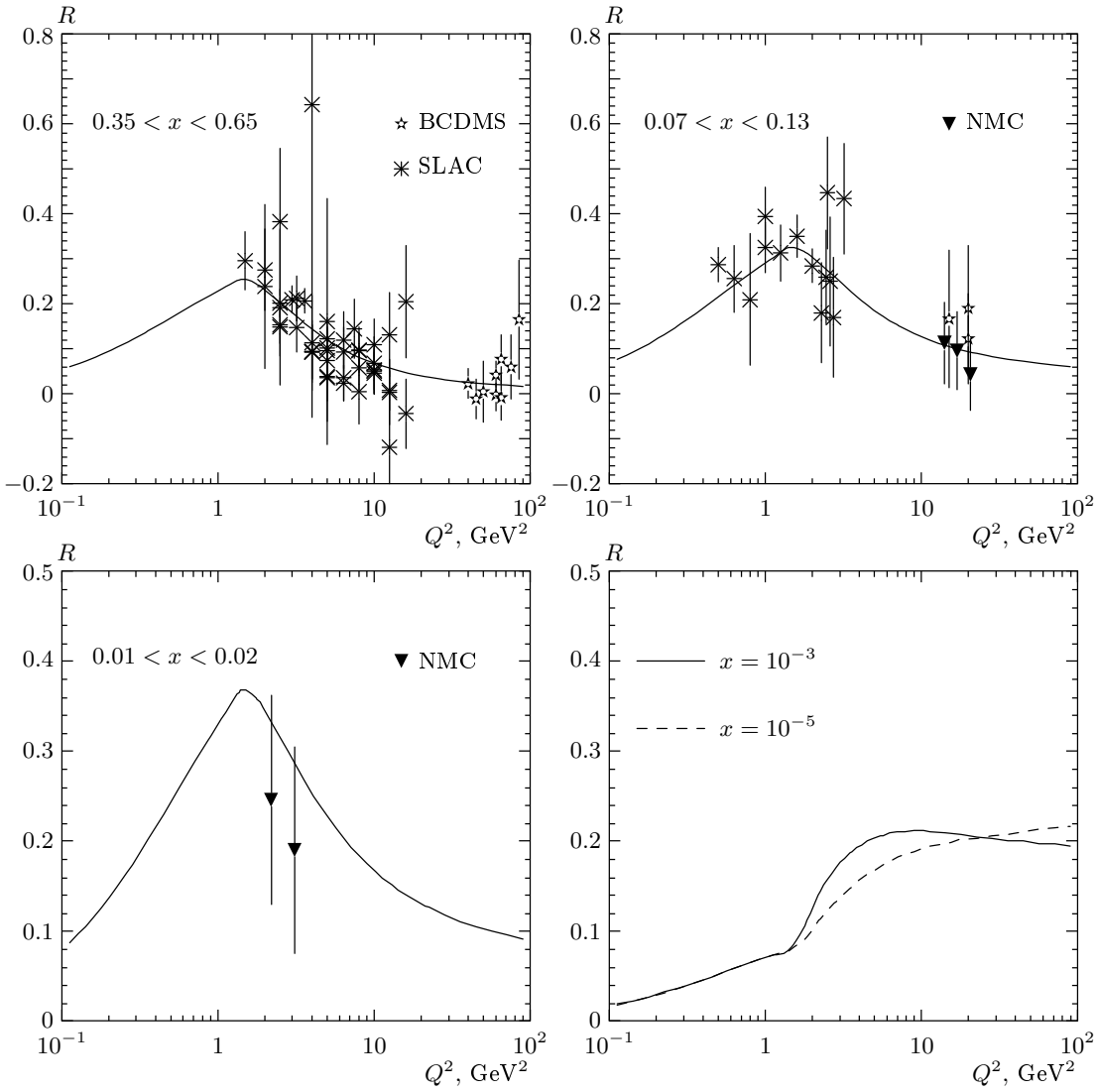

Fig. 9. The ratio $R(x, Q^2)$ as a function of Q^2 at fixed x. Data are from Refs. [5] and [20]

(i) Shadowing at x <0.1. The ratio $r^{A/d}$ is smaller than unity. The experimental data cover the region $x > 10^{-4}$ and $r^{A/d}$ decreases with decreasing x. Shadowing increases with the nuclear mass A and weakly depends on Q^2.

(ii) Antishadowing at $0.1 < x < 0.2$. The NMC data have established a small (several percent) but statistically significant excess over unity. Within the accuracy of the data, no significant Q^2-dependence of this effect has been found.

(iii) The EMC effect at $0.2 < x < 0.8$. The measured ratio $r^{A/d}$ decreases as x rises and has a minimum at $x = 0.6$. The magnitude of this depletion grows slowly with the nuclear mass number. The data imply that a strong Q^2-dependence of $r^{A/d}$ is also excluded in this region.

(iv) The Fermi motion. At $x > 0.8$, the ratio $r^{A/d}$ rises above unity, but experimental information is rather scarce.

Investigations of differences between the longitudinal-to-transverse cross-section ratio R for different nuclei showed that $R^{A_i} - R^{A_j}$ is compatible with zero. This implies that nuclear effects influence both structure functions, F_1 and F_2, in a similar way.

At the moment, there is no unique theoretical description of these effects; it is believed that different mechanisms are responsible for them in different kinematical regions. For example, the EMC effect indicates that the averaged momentum carried by valence quarks in nuclei is reduced relative to free nucleon. It has been

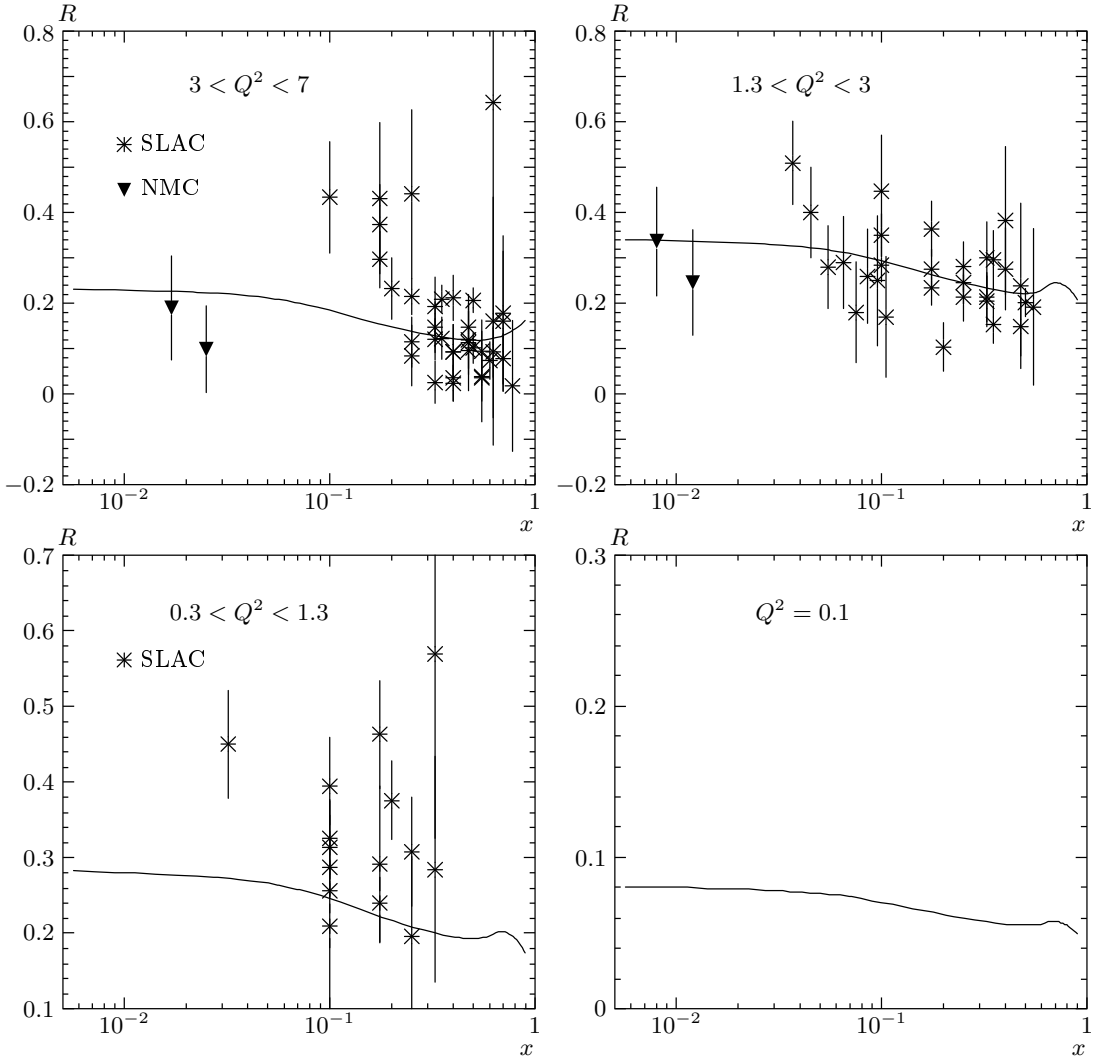

Fig. 10. The ratio $R(x, Q^2)$ as a function of x at fixed Q^2. Data are from [5, 20]

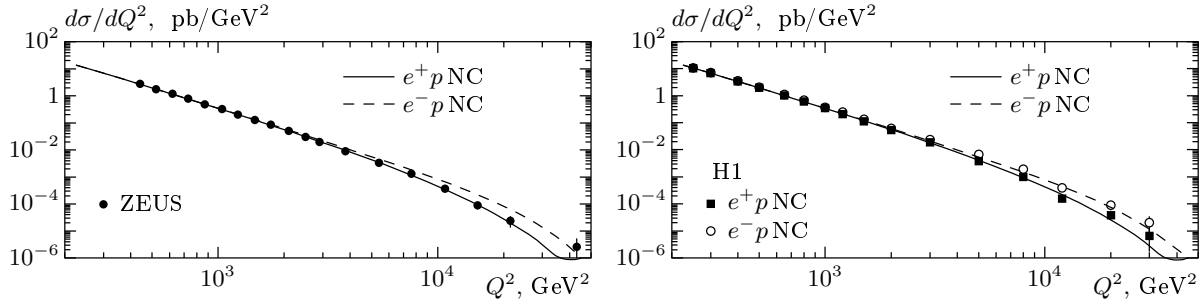

Fig. 11. The differential cross-section $d\sigma/dQ^2$ of the neutral current proton scattering off electron (positron) as a function of Q^2. Points are the results of ZEUS [22] and H1 [23] experiments

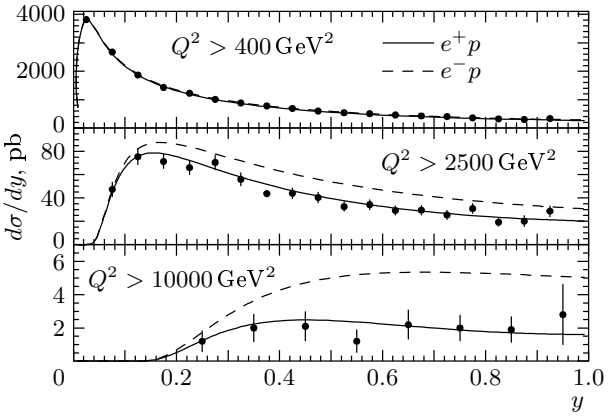

Fig. 12. The differential cross-section $d\sigma/dy$ of the neutral current proton scattering off electron (positron) as a function of y. Experimental data are due to ZEUS [22] experiment

shown [26] that the pattern of the function $r^{A/d}(x)$ has a universal shape in the range $10^{-3} < x < 0.96$ and for the mass of the nuclei $A \geq 4$. Namely, the ratio $F_2^A(x)/F_2^d(x)$ can be well approximated with phenomenological functions in different regions of x. At $x > 0.3$,

$$r^{A/d}(x) = 1 - m_b(A)a_{osc}(x), \tag{44}$$

where the A-dependence of m_b can be approximated as

$$m_b(A) = M_b\,[1 - N_s(A)/A] \quad \text{and} \quad M_b = 0.437 \tag{45}$$

for $A \neq 4$. The number of nucleons $N_s(A)$ at the nuclear surface is given by the Woods–Saxon potential,

$$N_s(A) = 4\pi\rho_0 \int\limits_{r_0(A)}^{\infty} \frac{r^2 dr}{1 + \exp\{[r - r_0(A)]/a\}}, \tag{46}$$

with the values of the parameters $\rho_0 = 0.17$ fm^{-3}, $a = 0.54$ fm, and

$$r_0(A) = 1.12A^{1/3} - 0.86A^{-1/3}. \tag{47}$$

The function $a_{osc}(x)$ is

$$a_{osc}(x) = (1-\lambda x)\left\{\left(\frac{1}{u} - \frac{1}{c}\right) - \mu\left(\frac{1}{u^2} - \frac{1}{c^2}\right)\right\}, \tag{48}$$

where $u = 1 - x$, $c = 1 - x_2$, x_2 =0.278, $\lambda = 0.5$, and $\mu = m_\pi/M$ (m_π is the pion mass). At $10^{-3} \leq x \leq 0.3$, the function is given by

$$r^{A/d}(x) = x^{m_1}(1 + m_2)(1 - m_3 x) \tag{49}$$

with

$$m_i = M_i\,[1 - N_s(A)/A]\,, \tag{50}$$

where $M_1 = 0.129$, $M_2 = 0.456$, and $M_3 = 0.553$. We used Eq. (49) to calculate $r^{A/d}$ up to $x_0 < 10^{-3}$.

The value of x_0 as a function of A was obtained as follows. The experimental data [26] show that in the region $5 \cdot 10^{-3} < x < 0.1$, the ratio $r^{A/d}$ decreases with x. Generally, small x correspond to small Q^2, and the approach of the real photon interaction can therefore be used. Hence, as $x \to 0$, $r^{A/d} \to \eta^A = \sigma_{\gamma A}/A\sigma_{\gamma N}$, where $\sigma_{\gamma A}$ is the photon-nuclear cross-section and $\sigma_{\gamma N}$ is the photon–nucleon cross-section averaged over proton and neutron. The expression for the function η^A has been obtained in Ref. [4] using the optical nuclear model,

$$\eta^A = 0.75G(z) + 0.25, \tag{51}$$

where

$$G(z) = \frac{3}{z^2}\left[\frac{z^2}{2} - 1 + e^{-z}(1 + z)\right] \tag{52}$$

and $z = 0.00282A^{1/3}\sigma_{\gamma N}(\nu)$. Using Eq. (34) with the values of parameters obtained in this work, we can write the averaged photon–nucleon cross-section as

$$\sigma_{\gamma N} = \frac{1}{2}(\sigma_{\gamma p} + \sigma_{\gamma n}) = \\ = 112.2\left(0.609\nu^{0.0988} + 1.037\nu^{-0.5944}\right). \tag{53}$$

In the range $x \ll 1$, Eq. (49) is reduced to

$$r^{A/d}(x) = x^{m_1}(1 + m_2). \tag{54}$$

From the asymptotic condition

$$r^{A/d}(x_0) = 0.75G(z) + 0.25, \tag{55}$$

we then obtain the expression for x_0:

$$x_0 = \left[\frac{1}{1 + m_2}\,(0.75G(z) + 0.25)\right]^{1/m_1}. \tag{56}$$

At $x < x_0$, we assumed that the function $r^{A/d}$ is constant and

$$r^{A/d}(x) = r^{A/d}(x_0). \tag{57}$$

The results of approximating the ratio $r^{A/d}$ are presented in Fig. 13 as functions of x for different nuclear targets and are in a good agreement with experimental data.

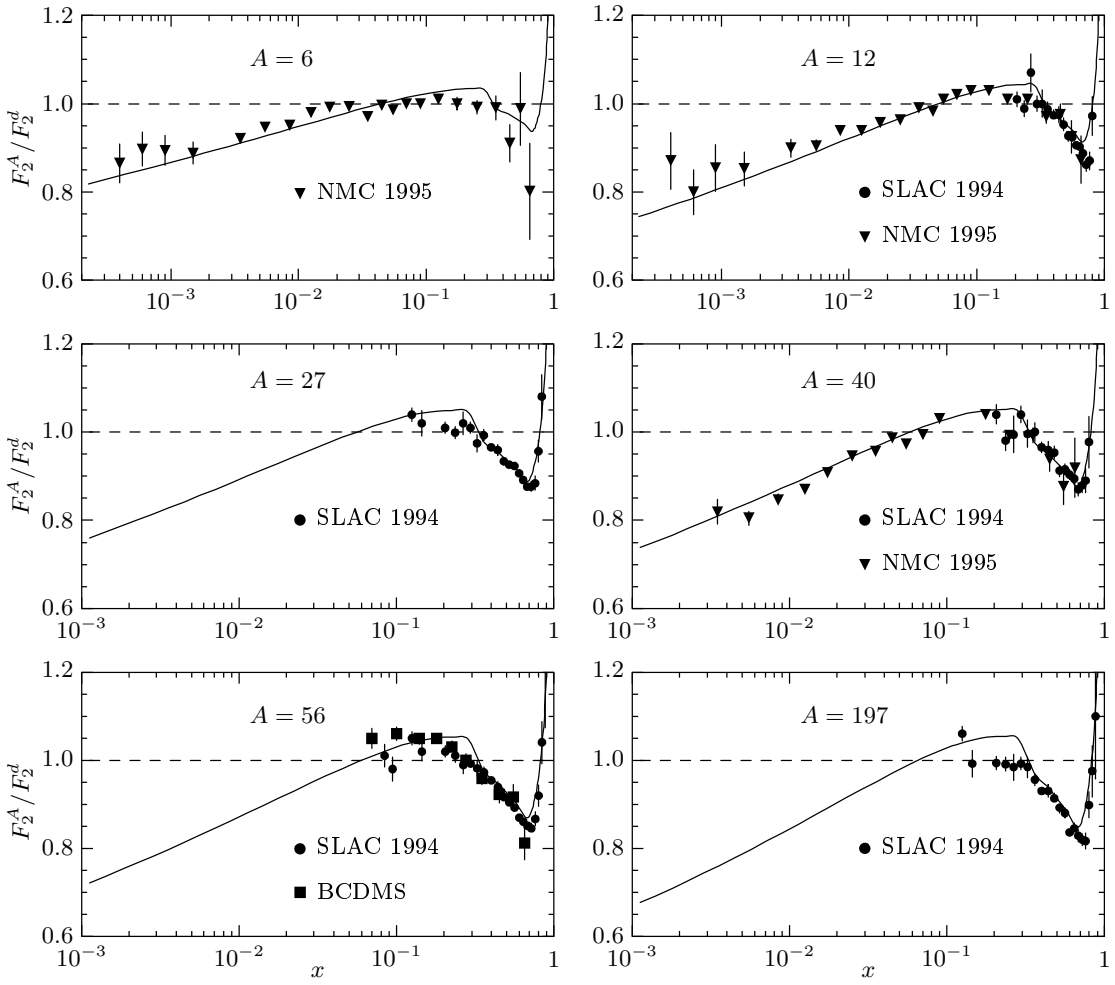

Fig. 13. The comparison of the ratio F_2^A/F_2^d measured by the SLAC, BCDMS, and NMC groups with the approximation given in [26] (solid lines)

Taking the nuclear effects into account, the nuclear structure functions $F_i(x,Q^2)$ and total photon-nuclear cross-section can be written as

$$F_i^A(x,Q^2) = Ar^{A/d}(x,A)F_i^N(x,Q^2) \qquad (58)$$

and

$$\sigma_{\gamma A}(\nu) = A\sigma_{\gamma N}(\nu)[0.75G(z) + 0.25]. \qquad (59)$$

The calculated cross-sections $\sigma_{\gamma A}(\nu)$ are shown in Fig. 14 as functions of the real photon energy for nuclei C, Cu, and Pb.

5. MUON INELASTIC SCATTERING IN THE STANDARD ROCK

We have calculated the main characteristics of the inelastic muon scattering in the standard rock ($A = 22$, $Z = 11$ and $\rho = 2.65$ g/cm^3). The spectra of the muon energy loss in a single interaction,

$$\frac{N_{Av}}{A}\nu\frac{d\sigma_{\mu A}}{d\nu} = \frac{N_{Av}}{A}\nu\int\limits_{Q^2_{min}}^{Q^2_{max}}\frac{d\sigma^2_{\mu A}}{d\nu dQ^2}dQ^2 \qquad (60)$$

(where N_{Av} is the Avogadro number), are shown in Fig. 15 as functions of the inelasticity y for different muon energies. The energy dependences of the total cross-section,

$$\sigma_{\mu A}(E) = \int\limits_{\nu_{min}}^{\nu_{max}}\frac{d\sigma_{\mu A}}{d\nu}d\nu, \qquad (61)$$

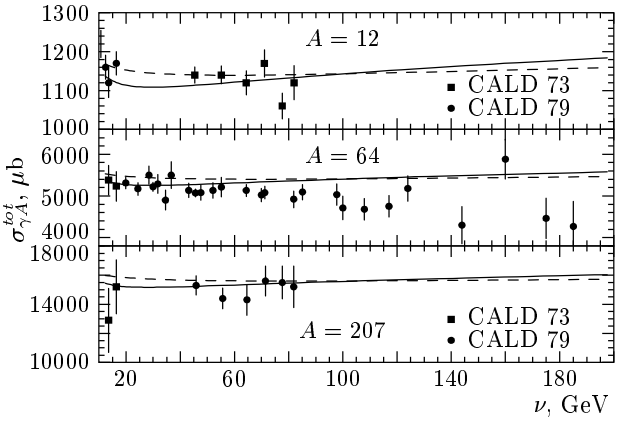

Fig. 14. The total cross-section $\sigma_{\gamma A}(\nu)$ for C, Cu, and Pb as a function of the real photon energy. Results of our calculations (solid curves) and calculations by Bezrukov and Bugaev [4] (dashed curves) as compared to experimental data [27]

and the muon energy loss

$$b_n(E) = \frac{N_{Av}}{A} \int\limits_{\nu_{min}}^{\nu_{max}} \nu \frac{d\sigma_{\mu A}}{d\nu} d\nu \qquad (62)$$

are shown in Fig. 16. The allowed kinematical region for the variables ν and Q^2 is determined by the equations

$$Q^2 = 2\,(EE' - |\mathbf{k}||\mathbf{k}'|\cos\theta) - 2m^2 \qquad (63)$$

with $\cos\theta = \pm 1$ and

$$Q^2 = 2M\nu + M^2 - W^2. \qquad (64)$$

The results in Ref. [4] are also given in these figures for comparison. We note that the cross-section and the muon energy loses [4] have been calculated taking only the shadowing effect into account. The cross-section of the inelastic muon scattering obtained in the present work is larger by the factor 1.2 and the muon energy loss $b_n(E)$ is also larger by about 8 % at $E = 10^3$ GeV and 30 % at $E = 10^6$ GeV. As a result, the total energy loss (the sum of bremsstrahlung, pair production, and inelastic muon scattering) increase by about 1 % at $E = 10^3$ GeV and 4 % at $E = 10^6$ GeV. These differences are mainly due to contributions of small x and small Q^2, where the modern structure functions are larger than that used by Bezrukov and Bugaev [4].

The probabilities $P(\geq\theta, \geq v)$ of the muon scattering in a single interaction at the angles larger than θ with the outgoing muon energy $E' \geq vE$ are shown in Fig. 17 as a function of θ for different values of v and primary muon energies. The results are given for the μ^- and μ^+ scattering. The main peculiarities of the inelastic muon scattering are as follows.

(i) At fixed values of θ and E', the probability decreases very rapidly with the initial muon energy E. For example, for $\theta \geq 2^\circ$ and $E' = 10$ GeV, we have $P = 6.3 \cdot 10^{-4}$ at $E = 10^2$ GeV and $P = 3.8 \cdot 10^{-6}$ at $E = 10^3$ GeV.

(ii) At fixed values of θ and E, the probability increases with decreasing the outgoing muon energy E'. For $\theta \geq 2^\circ$ and $E = 10^3$ GeV, we have $P = 7.8 \cdot 10^{-7}$ at $E' \geq 10^2$ GeV and $P = 3.8 \cdot 10^{-6}$ at $E' \geq 10$ GeV.

(iii) At fixed values of E and E', the mean values of x and Q^2 ($\langle x\rangle$ and $\langle Q^2\rangle$) increase with θ. For the muon energies $E = 10^2$ GeV and $E' \geq 0.1E$, the values of $\langle x\rangle$ and $\langle Q^2\rangle$ increase from $\langle x\rangle = 0.12$ (antishadowing region) and $\langle Q^2\rangle = 0.75$ GeV^2 at $\theta = 0.25^\circ$ up to $\langle x\rangle = 0.25$ (EMC region) and $\langle Q^2\rangle = 34$ GeV^2 at $\theta = 6^\circ$. For the energies $E = 10^3$ GeV and $E' \geq 0.1E$, we have $\langle x\rangle = 0.09$ (shadowing region), $\langle Q^2\rangle = 28$ GeV^2 at $\theta = 0.25^\circ$ and $\langle x\rangle = 0.46$ (EMC region) and $\langle Q^2\rangle = 925$ GeV^2 at $\theta = 6^\circ$. The probability of scattering at large angles is therefore suppressed by the EMC effect.

6. CONCLUSIONS

We have studied the inelastic muon scattering off nuclei.

1. It is shown that the combination of the structure function F_2 predicted by the CKMT model at low and moderate values of Q^2 and the MRS99 parton distribution functions at high Q^2 gives a good description of the data over the entire measured region from photoproduction to DIS. In particular, the CKMT model well describes the rise of F_2^p at low x and Q^2 with the slope $\Delta_0 = 0.0988$. Furthermore, the expression for the neutron structure function F_2^n can be obtained in the framework of this model. The result is in a good agreement with the F_p^2/F_n^2 and $F_p^2 - F_n^2$ data.

2. The MRS99 parton distribution functions well describe the differential cross-sections $d\sigma/dQ^2$ and $d\sigma/dy$ calculated taking not only the electromagnetic current contribution but also the contributions of the neutral current and the γ–Z interference into account. The γ–Z interference contribution is clearly seen at high $Q^2 > 10^3$ GeV^2.

3. The nuclear effects modify the nucleon structure functions in the entire measured region of x and

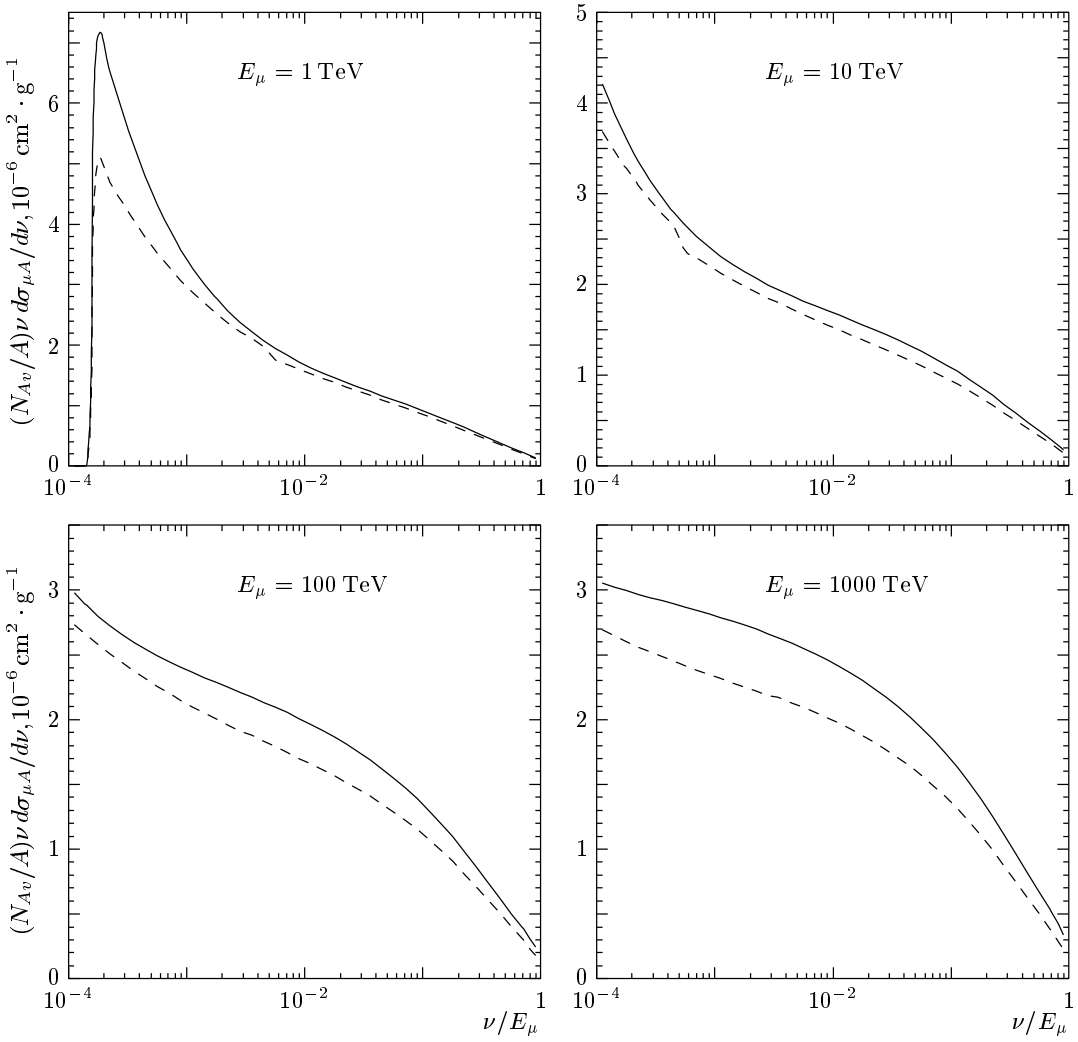

Fig. 15. The spectra of the muon energy loses due to the muon inelastic scattering in the standard rock ($A = 22$, $Z = 11$) as a function of y for fixed muon energies, as compared to calculations by Bezrukov and Bugaev [4] (dashed line)

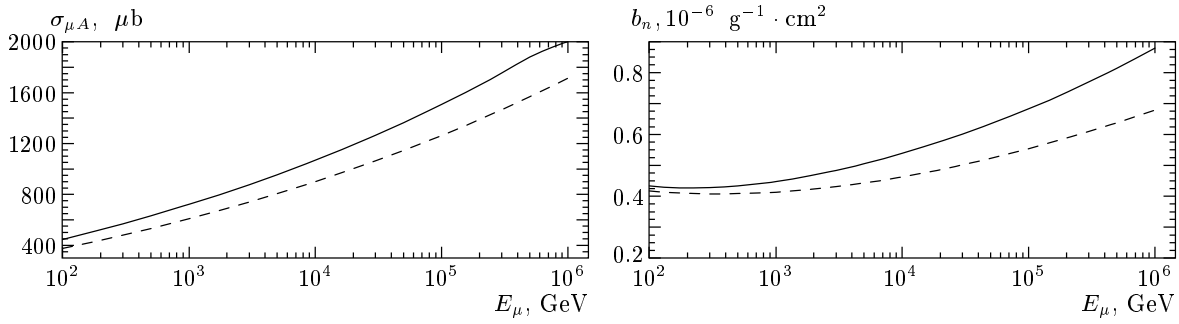

Fig. 16. The total cross-section $\sigma_{\mu A}$ and the muon energy loss b_n for the muon inelastic scattering in the standard rock ($A = 22$, $Z = 11$) as a function of the muon energy E_μ, as compared to those in Ref. [4] (dashed line)

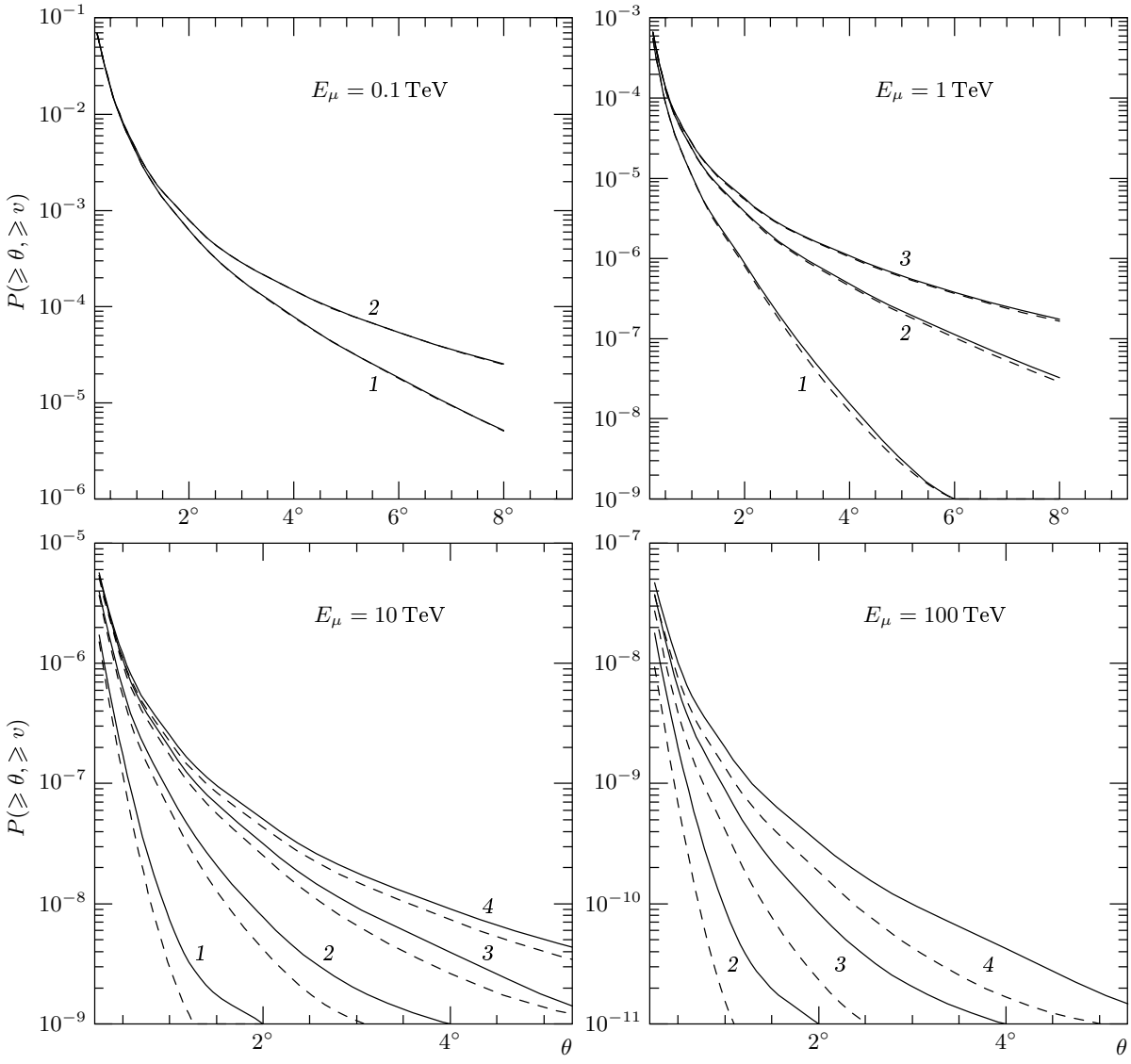

Fig. 17. The probabilities $P(\geq \theta, \geq v)$ of the muon scattering in a single interaction in the standard rock ($A = 22$, $Z = 11$) at an angle larger than θ with the outgoing muon energy $E' \geq vE$ as a function of θ for fixed values of the incoming muon energies and v: *1* — $v \geq 10^{-1}$; *2* — $v \geq 10^{-2}$; *3* — $v \geq 10^{-3}$; *4* — $v \geq 10^{-4}$. Solid (dashed) lines are for a positive (negative) muon charge

Q^2. The modification depends on Q^2 very slightly and increases with A.

4. The obtained structure functions have been used for calculations of the muon–nucleus scattering cross-section, muon energy losses, and muon angular distributions in inelastic interactions. The nuclear effects and contributions of the neutral current and γ–Z interference were taken into account. As a result, the total cross-section and energy losses increase with the muon energy faster than predicted in Ref. [4]. The scattering of high-energy muons ($E > 10^3$ GeV) at large angles is suppressed by both the EMC effect and γ–Z interference.

We are grateful to A. B. Kaidalov and F. V. Tkachev for helpful discussions. This work was supported by the Russian Foundation for Basic Research (project 99-02-18374).

REFERENCES

1. K. Kobayakawa, Nuovo Cimento B **47**, 156 (1967).

2. P. Ditsas, B. J. Read, and G. Shaw, Nucl. Phys. B **99**, 85 (1975).

3. P. Ditsas and G. Shaw, Nucl. Phys. B **113**, 246 (1976).

4. L. B. Bezrukov and E. V. Bugaev, Sov. J. Nucl. Phys. **33**, 635 (1981).

5. http://
www-spires.dur.ac.uk/HEPDATA/structure.html

6. A. Capella, A. Kaidalov, C. Merino, and J. Tran Thanh Van, Phys. Lett. B **337**, 358 (1994).

7. A. D. Martin, R. G. Roberts, W. J. Srirlind, and R. S. Thorne, Eur. Phys. J. C **14**, 133 (2000).

8. M. Gluck, E. Reya, and A. Vogt, Eur. Phys. J. C **5**, 461 (1998).

9. H. L. Lai, J. Huston, and S. Kuhlmann, Eur. Phys. J. C **12**, 375 (2000).

10. D. Schildknecht, Acta Phys. Polon. B **28**, 2453 (1997).

11. H. Abramowicz and A. Levy, E-print archives hep-ph/9712415.

12. K. Abel, F. Barreiro, and F. J. Yndurain, E-print archives hep-ph/9610380; K. Abel and F. J. Yndurain, Nucl. Phys. B **495**, 221 (1997).

13. A. M. Cooper-Sarkar, R. Devenish, and A. De Roeck, Int. J. Mod. Phys. A **13**, 3385 (1998).

14. C. Merino, A. B. Kaidalov, and D. Pertermann, Eur. Phys. J. C **20**, 301 (2001).

15. J. Breitweg et al. (ZEUS Collaboration), Phys. Lett. B **487**, 53 (2000).

16. D. O. Caldwell, J. P. Cumalat, and A. M. Eisner, Phys. Rev. **40**, 122 (1978).

17. M. Derrick et al. (ZEUS Collaboration), Z. Phys. C **63**, 391 (1994); S. Aid et al. (H1 Collaboration), Z. Phys. C **69**, 27 (1995); J. Breitweg et al. (ZEUS Collaboration), Eur. Phys. J. C **7**, 609 (1999).

18. M. Arneodo et al. (New Muon Collaboration), Phys. Rev. D **50**, R1 (1994).

19. M. Arneodo et al. (New Muon Collaboration), Nucl. Phys. B **487**, 3 (1997); L. H. Tao, L. Andivahis, P. L. Anthony et al. (E143 Collaboration), Z. Phys. C **70**, 83 (1996).

20. K. Abe, T. Akagi, and P. L. Anthony (E143 Collaboration), Phys. Lett. B **452**, 194 (1999).

21. A. D. Martin, M. G. Ryskin, and A. M. Stasto, Eur. Phys. J. C **7**, 643 (1999).

22. J. Breitweg et al. (ZEUS Collaboration), Eur. Phys. J. C **11**, 427 (1999).

23. C. Adloff et al. (H1 Collaboration), Eur. Phys. J. C **13**, 609 (2000); C. Adloff et al., Eur. Phys. J. C **19**, 269 (2001).

24. M. Arneodo, Phys. Rep. **240**, 301 (1994).

25. G. Piller and W. Weise, Phys. Rep. **330**, 1 (2000).

26. G. I. Smirnov, Phys. Lett. B **364**, 87 (1995); G. I. Smirnov, Eur. Phys. J. C **10**, 239 (1999).

27. D. O. Caldwell, V. B. Elings, and W. P. Hesse, Phys. Rev. D **7**, 1362 (1973); D. O. Caldwell, J. P. Cumalat, and A. M. Eisner, Phys. Rev. Lett. **42**, 553 (1979).